# Argon Plasma Treatment to Tune Perovskite Surface Composition for High Efficiency Solar Cells and Fast Photodetectors

*Xun Xiao, Chunxiong Bao, Yanjun Fang, Jun Dai, Benjamin R. Ecker, Congcong Wang, Yuze Lin, Shi Tang, Ye Liu, Yehao Deng, Xiaopeng Zheng, Yongli Gao, Xiao Cheng Zeng, and Jinsong Huang\**

**The surface composition of perovskite films is very sensitive to film processing and can deviate from the optimal, which generates unfavorable defects and results in efficiency loss in solar cells and slow response speed in photodetectors. An argon plasma treatment is introduced to modify the surface composition by tuning the ratio of organic and inorganic components as well as defect type before deposition of the passivating layer. It can efficiently enhance the charge collection across the perovskite–electrode interface by suppressing charge recombination. Therefore, perovskite solar cells with argon plasma treatment yield enhanced efficiency to 20.4% and perovskite photodetectors can reach their fastest respond speed, which is solely limited by the carrier mobility.**

Organic–inorganic halide perovskite (OIHP) have attracted extensive research interest for the next generation solar cells due to their promising optoelectronic properties, such as large light absorption coefficient, high charge carrier mobility as well as long carrier recombination lifetime.[1–3] The power conversion efficiency (PCE) of OIHP solar cells quickly rose from 3% at the initial stage to over 20% after development for a few years.[4–8] Passivation of defects at film surface and grain boundaries (GBs) has been shown to play an important

role in the efficiency enhancement.[9–14] Many efforts have been devoted in the past few years to enlarge grains of polycrystalline perovskite films to reduce the GB area.[5,15–17] For example, grains with large aspect ratio were grown on a nonwetting surface, and thus to reduce the charge recombination in the devices.[15,18] Now that the surface of perovskite films might be much more defective than GBs and surface area is much larger GB area, passivating the film surface to reduce the nonradiative recombination at perovskite surface is critically needed for high device efficiency.[19–22]

The surface defects in OIHP materials are charged due to the ionic nature of OIHP materials, in comparison with the dangling bonds in traditional semiconductor material such as Si,[23–25] which required different passivation methods. To date, many materials have been reported to interact with the charged defects as electron or hole acceptors to passivate the relevant charge traps.[21,26–28] For example, $\pi$-conjugated Lewis base was introduced,[29] a type of organic semiconducting molecules attached with Lewis base blocks, could effectively passivate the Lewis acid traps such as undercoordinated Pb ions and Pb clusters.[30,31] However, most passivation molecules could only passivate limited types of defects. For example, phenyl-C61-butyric acid methyl ester ($PC_{61}BM$) could effectively passivate some lead-based defects such as Pb–I antisite and undercoordination of Pb atoms.[26,27] However, the common deep traps on the surface of perovskite films could be more complicated, including $Pb_i$, Pb cluster, and $I_{MA}$.[32] If the organic part, such as MA cation and I anion, could be removed, the $I_{MA}$ might be removed and the left lead-rich perovskite surface could be passivated efficiently by known electron transport materials such as fullerenes. Thermal annealing was used to remove methylammonium iodide (MAI) to tune the film composition.[33] However, due to the easy decomposition of $MAPbI_3$ under thermal annealing, the decomposition may occur far below the surface where the charge transport layer cannot reach and thus cause severe charge recombination.[34,35]

Here, we report an argon plasma treatment (APT) as an effective way to fine tune the surface composition of the perovskite thin films as well as single crystals. The APT can effectively remove the organic component of the perovskite surface,

X. Xiao, Dr. Y. Lin, Y. Deng, Prof. J. Huang
Department of Applied Physical Sciences
University of North Carolina
Chapel Hill, NC 27599, USA
E-mail: jhuang@unc.edu
X. Xiao, Dr. C. Bao, Dr. Y. Fang, Dr. Y. Lin, S. Tang, Y. Liu, Y. Deng,
X. Zheng, Prof. J. Huang
Department of Mechanical and Materials Engineering
University of Nebraska-Lincoln
NE 68588, USA
Dr. J. Dai, Prof. X. C. Zeng
Department of Chemistry
University of Nebraska-Lincoln
NE 68588, USA
B. R. Ecker, C. Wang, Prof. Y. Gao
Department of Physics and Astronomy
University of Rochester
Rochester, NY 14627, USA

1705176 (1 of 7)

**ADVANCED**
**SCIENCE NEWS**
www.advancedsciencenews.com

**ADVANCED**
**MATERIALS**
www.advmat.de

which unifies the defects type and leaves the lead-rich perovskite surface before the deposition of passivating layer for a better passivating effect.

APT is a common method to clean organic contaminant from the surface of materials with energetic argon plasma.[36–38] When applying plasma treatment to perovskite surface, we expect the argon plasma to remove the contaminants and partial of the organic component of the hybrid perovskite materials from the surface, such as methylammonium. It could form a lead-rich surface and uniform the defects type with lead-based defects exposed, while these defects were shown to be effectively passivated by passivating layer such as fullerene.[39–41] **Figure 1**a illustrated the process of APT for perovskite surface to remove organic component. In detail, high-energy argon plasma was produced by a radio frequency (RF) power source at frequency of 13.56 MHz to sputter-etch the perovskite surface, which broke the chemical bonds of organic component. Plasma treatment helped to remove the contamination, and remove organic part of the perovskite surface such as MA anions and I cations. The inorganic lead ions should remain, since they were difficult to remove by plasma. To analysis the effect of APT to modify the surface composition, x-ray photoelectron spectroscopy (XPS) measurements were made on samples that received progressive APT and the measurement results for the C 1s, N 1s, I 3d$_{5/2}$, and Pb 4f$_{7/2, 5/2}$ core levels were shown in Figure S1 of the Supporting Information. Due to instrumental limitations, different treatment times and powers compared to the device treatments were necessary for the in situ generated DC argon plasma used in the photoemission studies. The notable change observed was the development of a new spectral component in the Pb 4f$_{7/2, 5/2}$ spectra. The initial perovskite Pb 4f$_{7/2}$ component was located at 138.87 eV, and the new component developed at 137.22 eV after the first 10 s of APT and continued to grow in intensity with additional treatments relative to the perovskite Pb component (Pb perovskite). This new feature could be attributed to metallic lead (Pb (M)), and was likely created as the chemical bond between the lead and the surrounding iodine were disrupted and broken by the long time APT. While the metallic Pb component grew in intensity, the signal intensities for the other core levels, C 1s, N 1s, and I 3d$_{5/2}$, were rapidly decreasing relative to the overall lead signal
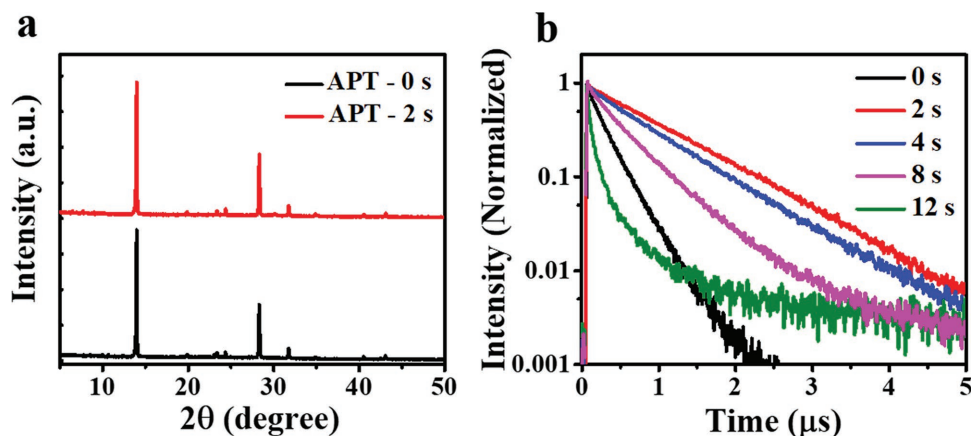
with increasing APT. It was helpful here to describe these changes in relative intensities by computing the surface's elemental ratio or empirical formula, where we normalized the elements ratio to the sum of the perovskite and metallic Pb signal as Pb was not particularly volatile in the ultra-high-vacuum (UHV) chamber. This could be seen in the elemental ratio plot (Figure 1b). The ideal C:N:I:Pb (perovskite):Pb (M) ratio for perovskite should be 1.0:1.0:3.0:1.0:0.00, and before APTs the ratio was 2.67:0.36:3.36:1.00:0.00. However, after the full 70 s of in situ APT the ratio was then 0.93:0.00:0.48:1.96:0.61:0.39 and this suggests that the APT was effectively removing the adventitious carbon, methylammonium, and iodide ions, perhaps as volatile components in the UHV chamber.

To further investigate the effect of APT on morphology, scanning electron microscopy (SEM) was carried out. From the SEM images, the perovskite films of APT-0s (Figure S2a, Supporting Information) and APT-2s (Figure S2b, Supporting Information) were both pinhole-free and smooth. There was no obvious difference observed on the top-view SEM images, which indicated the plasma treatment only changed the top surface without damaging the whole perovskite film. X-ray diffraction (XRD) was applied to determine the products of the APT (**Figure 2**a). As indicated by XPS test, the metallic lead would appear during the APT. However, films with APT-0s and APT-2s did not show peaks for metallic lead, which also indicated that the APT for 2 s could only affect the top surface of perovskite films rather than the whole layer. And when we increased the treatment time to 300 and 600 s, the peaks at 31.5° and 36.3°, which were assigned to metallic lead, showed up (Figure S3, Supporting Information). This was in agreement with XPS results.

Apart from the morphology, time-resolved photoluminescence (TRPL) for perovskite films with APT for different time (0, 2, 4, 8, 12 s) was applied to analysis carrier recombination process. Samples were excited by a 404 nm pulsed diode laser with a pulse width of 45 ps. As shown in Figure 2b, the pristine perovskite film with APT for 0 s had a decay time of 297 ns derived from a single exponential decay function fitting. The much longer PL lifetime of the APT-2s film was observed and fitted with a decay of 970 ns. The increase of PL lifetime is not well understood yet. It could be explained by the removal of
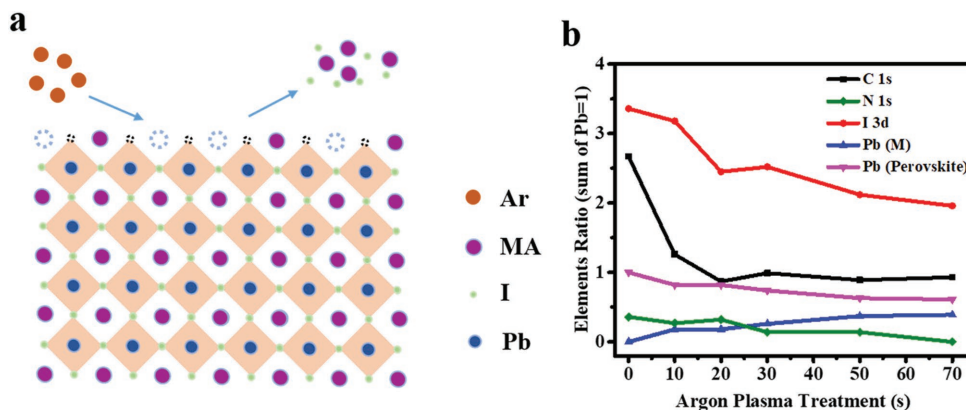


**Figure 1.** a) Scheme of argon plasma treatment (APT) for MAPbI$_3$ surface to remove MAI and expose lead rich surface. b) Elements ratio of perovskite films with in situ APT for different time (10, 20, 30, 50, and 70 s).

**ADVANCED
SCIENCE NEWS**
www.advancedsciencenews.com

**ADVANCED
MATERIALS**
www.advmat.de

**Figure 2.** a) X-ray diffraction patterns of MAPbI$_3$ films with argon plasma treatment for 0 and 2 s. b) TRPL spectrum of MAPbI$_3$ films with argon plasma treatment for different time (0, 2, 4, 8, 12 s).

excess organic component such as methylammonium interstitials, or other PL-quenching surface contaminants. It may also be caused by the exposed lead defects, such as lead cluster,[41] which were passivated by oxygen in the air efficiently since the TRPL was measured in ambient condition.[10] Nevertheless, when we further increased the treatment time, the PL lifetime showed a downward trend to 893, 556, and 127 ns after APT for 4, 8, and 12 s, respectively. The decrease of PL lifetime indicated that more nonradiative recombination centers showed up at the perovskite film surface, which should be caused by plasma-induced damage of the surface. TRPL analysis demonstrated that proper APT is helpful to reduce the nonradiative recombination on the surface and too-long treatment would cause film damaged.

The XPS measurement suggested the APT significantly influenced the perovskite surface elements ratio, and thus we expected APT should also impact device performance. **Figure 3**b showed current density–voltage ($J$–$V$) curves of perovskite solar cells based on the structure of indium tin oxide (ITO)/poly(bis(4-phenyl)(2,4,6-trimethylphenyl)amine) (PTAA)/perovskite/PC$_{61}$BM/C$_{60}$/bathocuproine (BCP)/ Cu as shown in Figure 3a with APT for different time. The control device with APT for 0 s showed open circuit voltage ($V_{oc}$) of 1.05 V and short-circuit current density ($J_{sc}$) of 21.2 mA cm$^{-2}$ as well as the fill factor (FF) of 0.73 and thus PCE of 16.3%, which represented a typical performance of control perovskite solar cells based on the structure shown by Figure 3a.[22] As shown in Figure 2b, for devices with APT for 2 s, the device yielded a highest efficiency with $V_{oc}$ of 1.11 V and $J_{sc}$ of 22.5 mA cm$^{-2}$ as well as FF of 0.816 and PCE of 20.4% compared with the control device with argon plasma for 0 s. This enhancement could be explained by the fact that the argon plasma could effectively remove the surface contamination and part of the methylammonium as well as iodide. As a result, the remained lead rich surface exposed the lead defects such as lead interstitial and lead cluster buried by the organic components, which could be passivated by PC$_{61}$BM more efficiently. When the APT duration increased to 4, 8, and 12 s, the PCE were 18.4%, 17.5%, and 14.2%, respectively. The reduced PCE mainly came from the loss of $J_{sc}$ and FF, which might be the result of long plasma treatment induced MAPbI$_3$ decomposition, and thus increased charge recombination at

the surface. Figure 3c showed the external quantum efficiency (EQE) spectrum of perovskite solar cells with APT for 2 and 0 s. The enhanced EQE over whole absorption region of wavelength from 300 to 800 nm with APT for 2 s compared with 0 s could be explained by the removal of organic part exposed defects like lead interstitial and lead cluster, which could be passivated by fullerene passivating layer more efficiently. This would be helpful for suppressing the surface charge recombination and thus enhancing the EQE. The statistics of PCE were presented in Figure 3d, which indicated the reliability and repeatability of efficiency improvement by using the APT with an average PCE at 19.3%. Figure 3e exhibited the steady-state output at maximum power point at the bias of 0.95 V. Figure 3f showed the $J$–$V$ curves of the device stored in air for 336 h. The device kept 90% of its initial efficiency after stored in ambient condition for 336 h with an average humidity of 50%.

To gain insight about how APT affects the trap passivation and the charge recombination process in the operating devices, transient photocurrent (TPC) and transient photovoltage (TPV) measurement of perovskite solar cells were carried out. For the TPC measurement, the devices were under room light and laser pulses (337 nm 4 ns) were conducted to trigger a small photocurrent signal. We could fit the current decay curve to get the charge transport lifetime. As shown in **Figure 4**a, for the control device with argon plasma for 0 s, the fitting charge transport time was 166 ns. The carrier transport time in a solar cell was determined by either carrier transit time, carrier trapping/ detrapping time, or RC constant of the device, whichever was longer. Our previous study showed that the carrier transit time in 500 µm thick perovskite layer was less than 1 ns, while the RC constant of the device with the present area was below 100 ns.[42] Thus a longer TPC lifetime than RC constant indicated that the charge traps in the device limited the carrier extraction process. The charge transport time reduced to 85 ns for the device with APT for 2 s, which was almost limited by RC constant. It proved that APT together with fullerene passivation could effectively passivate surface charge traps to an extent so that the residual charge traps did not notably affect the charge collection process. Figure 4b showed the TPV results of the devices with argon plasma for 2 and 0 s, respectively. For the TPV test, the devices were placed under AM 1.5 simulated illumination. And

**ADVANCED
SCIENCE NEWS**

www.advancedsciencenews.com

**ADVANCED
MATERIALS**

www.advmat.de
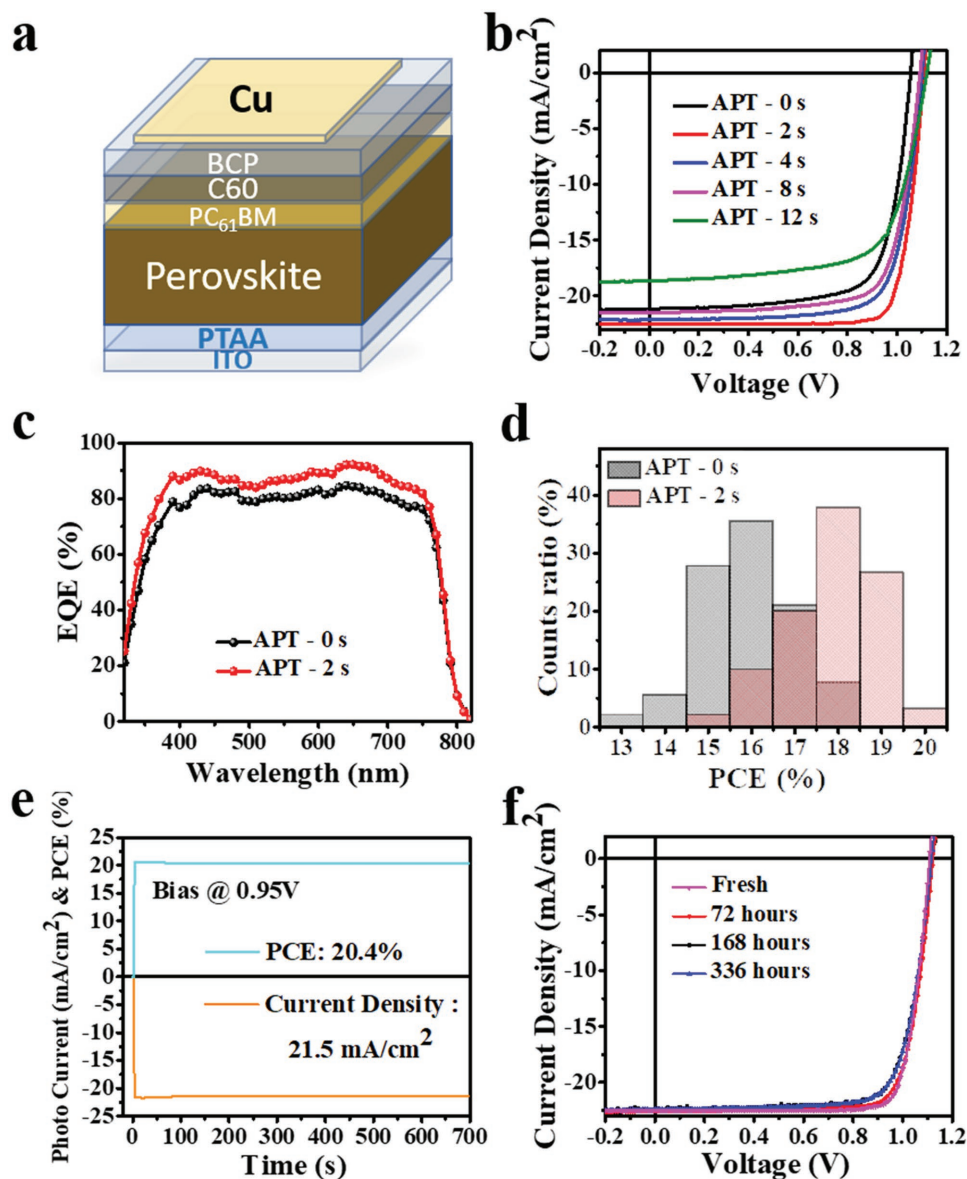
**Figure 3.** a) Device structure diagram. b) $J$–$V$ curves and c) EQE of the devices with argon plasma treatment for different time, and d) statistic of distribution of PCE. e) Steady-state measurement of $J_{sc}$ and PCE of best device with argon plasma for 2 s and f) the stability test of the best device exposed to air without encapsulated. The average humidity of atmosphere was about 50%.

the same laser pulse with TPC measurement was applied to trigger a small photovoltage. Based on the fitting of TPV decay, the charge recombination lifetime of devices with APT for 2 s was increased to 528 ns from 415 ns for the control device, which indicated that charge recombination was suppressed with APT for 2 s. The TPV results also indicated that the device with APT for 2 s had a larger average photovoltage of 1.11 V than 1.05 V of the control device with APT for 0 s, which was in accordance with the photocurrent measurement.

In addition, we applied APT to the thin single crystal device with the structure of ITO/PTAA/MAPbI$_3$/PC$_{61}$BM/C$_{60}$/BCP/Cu with an aim to achieve fast single crystal perovskite detectors. It has been demonstrated by us and others that there is a much

higher density of charge traps on single crystals surface.[43,44] Here, the MAPbI$_3$ thin crystal was grown by a recently developed hydrophobic interface confined lateral crystal growth method[45] so that its thickness can be as thin as tens of μm.[46] As shown in Figure 4c,d, the TPC lifetime was in the order of > 1 μs for a device with 15 μm thick MAPbI$_3$ crystal. The carrier transit time in such crystal was calculated to be 15 ns based on a carrier mobility of 150 cm$^2$ V$^{-1}$ s$^{-1}$, and build-in potential of 1 V. This again indicated the presence of a large density of charge traps at the surface of these MAPbI$_3$ crystals. The APT could effectively reduce the TPC time by almost 100-fold to 15 ns, which is now only determined by the carrier transit time through the thin single crystals. This confirmed that the

**ADVANCED**
**SCIENCE NEWS**
www.advancedsciencenews.com

**ADVANCED**
**MATERIALS**
www.advmat.de
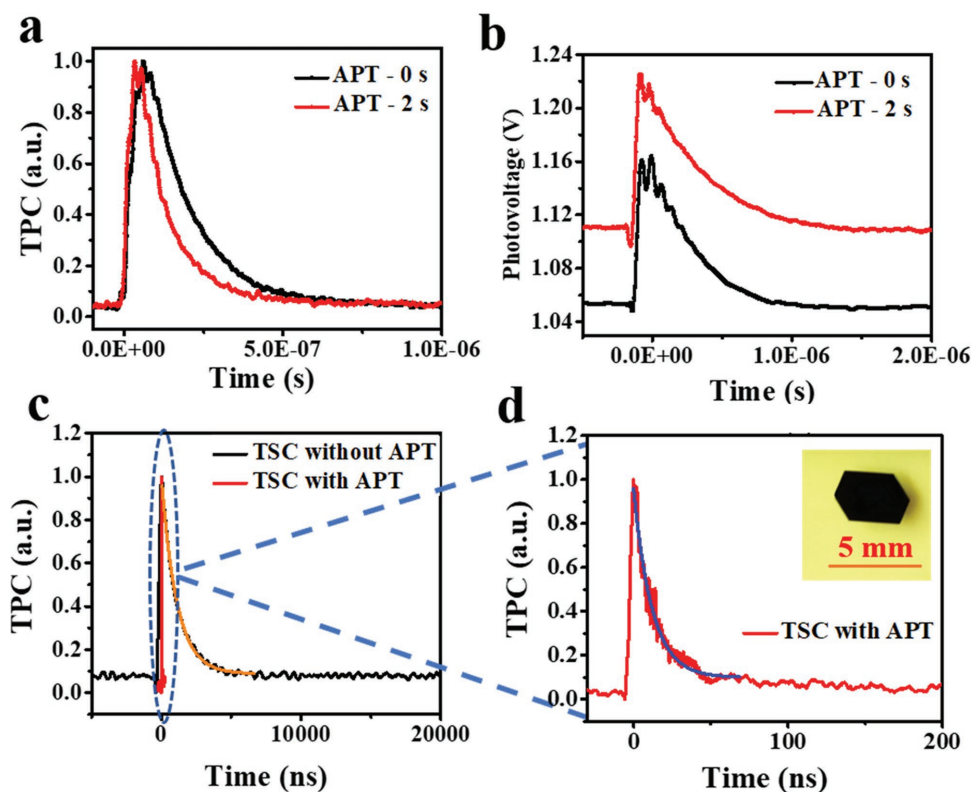
**Figure 4.** a) TPC and b) TPV of perovskite solar cells with argon plasma treatment for 0 and 2 s. c) TPC of thin single crystal (TSC) device without argon plasma treatment (black line) and with argon plasma treatment (red line) and fitting curve (orange line). d) zoom-in of (c). Inset is the photograph of thin single crystal. e) Computed density of states (DOS) of the excess MAI-terminated MAPbI$_3$ surface with Pb clusters, and with the passivated surface by PCBM. f) Trap density of states (tDOS) for device with argon plasma treatment for 0 and 2 s.

APT could effectively get rid of trapping and detrapping process caused by surface traps and thus achieve high speed single crystal perovskite photodetectors.

Finally, we studied the mechanism why APT combining with fullerene can effective passivate the charge traps. Density functional theory (DFT) calculations were applied to find out the effect of the excess MAI by computing the density of states with and without excess MAI on MAPbI$_3$ surface. As shown in **Figure 5**a,b, when passivated with PC$_{61}$BM, the trap states from

the undercoordinated Pb clusters were reduced in both with and without excess MAI models, becoming much shallower (Note: the shifts are comparable in both models). By contrast, a shrink of the band gap in the model with excess MAI was predicted upon the absorption of PC$_{61}$BM, while in the model without excess MAI, the band gap of the model was well maintained. This was because the valence band edge was from the top MAI layer, and the interaction between MAI and PC$_{61}$BM was stronger in the model with excess MAI. We also found direct
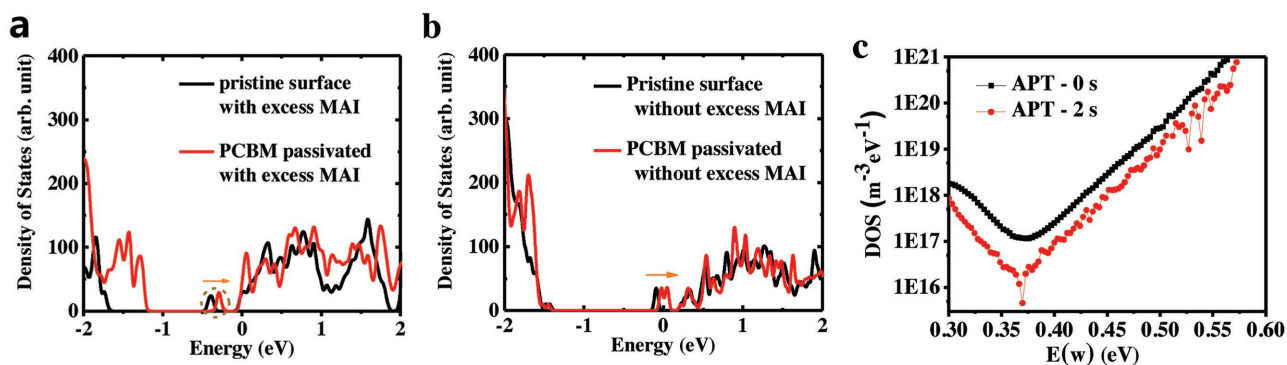


**Figure 5.** a) Computed density of states (DOS) of the excess MAI-terminated pristine MAPbI$_3$ surface with excess MAI and Pb cluster, and with the passivated surface by PCBM. b) Computed density of states (DOS) of the excess MAI-terminated MAPbI$_3$ pristine surface without excess MAI and with Pb clusters, and with the passivated surface by PCBM. c) Trap density of states (tDOS) for device with argon plasma treatment for 0 and 2 s.

**ADVANCED
SCIENCE NEWS**

www.advancedsciencenews.com

**ADVANCED
MATERIALS**

www.advmat.de

evidences for enhancing passivation efficiency of APT by measuring the trap density of states (tDOS) of the devices with APT by thermal admittance spectroscopy (TAS), which is a well-established and effective technique for characterizing both shallow and deep defects of thin film solar cells.[26,47–49] As shown in Figure 5c, the device with APT for 2 s had lower tDOS over the whole trap depth region. The device with APT had low tDOS in deep trap region (>0.4 eV), which was assigned to defects at the film surface. And the density of shallower trap states (<0.40 eV) was assigned to traps at GBs. The lower trap states in the shallower trap region of devices with APT for 2 s indicated that the treatment might help the fullerene to diffuse into the grain boundaries to passivate the shallow trap located at GBs as well as passivate the deep trap at the surface.

In summary, we introduced APT into the fabrication process of perovskite solar cells to tune the surface composition and uniform the surface defects type by removal of surface organic component. The uniformed defects could be effectively passivated by passivating layer. Perovskite solar cells with APT for 2 s showed an improved performance with average PCE of 19.3% and best PCE of 20.4%. And TSC photodetectors with APT showed almost 100-fold quicker response speed compared with control devices. There still have room to further improve the passivation effect since the PL lifetime is still lower than that of single crystals.

## Experimental Section

*Perovskite Fabrication*: The two-step method made MAPbI$_3$ films were fabricated by thermal annealing-induced interdiffusion method according to the previous publication.[16,50,51] The hole transport layer poly(bis(4-phenyl)-(2,4,6-trimethylphenyl)amine) (PTAA) with concentration of 2 mg mL$^{-1}$ dissolved in toluene were spin-coated at the speed of 6000 rpm for 35 s and then annealed at 100 °C for 10 min. PbI$_2$ beads (99.999% trace metals basis) were purchased from Sigma-Aldrich. After dissolved in *N,N*-dimethylformamide (DMF) at temperature of 100 °C, around 50 μL of hot (≈90 °C) 630 mg mL$^{-1}$ PbI$_2$ DMF precursor solutions was quickly dropped onto the substrate and spin-coated at the speed of 6000 rpm. The as-fabricated PbI$_2$ films were dried and annealed at 90 °C for 10 min. After the PbI$_2$ films cooled to 70 °C, 60 μL of 63 mg mL$^{-1}$ MAI 2-propanol precursor solution at the temperature of 70 °C was spun on the PbI$_2$ films. Subsequently, the sample was annealed at 70 °C for 20 min and 100 °C for 60 min. During the thermal annealing process, around 10 μL of DMF was added to the edge of the petri dish when the temperature reached 100 °C.

*Argon Plasma Treatment*: Argon plasma was produced by RF excitation with a power source of 13.56 MHz (Plasma Etch PE25-JW plasma etching/cleaning system) for argon plasma treatment. The power of RF excitation was tuned to 240 W.

*Device Characterization*: Simulated AM 1.5G irradiation (100 mW cm$^{-2}$) was produced by a Xenon-lamp-based solar simulator (Oriel 67005, 150 W Solar Simulator) for *J–V* measurements. The light intensity was calibrated by a silicon (Si) diode (Hamamatsu S1133) equipped with a Schott visible-color glass-filtered (KG5 color-filtered). Keithley 2400 Source-Meter was used for *J–V* measurement. The scanning rate was 0.1 V s$^{-1}$. The steady-state $V_{OC}$ and $J_{SC}$ were measured by zero bias current and zero bias voltage versus time, respectively. The steady-state PCE was measured by monitoring current with largest power output bias voltage and record the value of photocurrent. XRD measurements were performed with a Rigaku D/Max-B X-ray diffractometer with Bragg-Brentano parafocusing geometry, a diffracted beam monochromator, and a conventional cobalt target X-ray tube set to 40 kV and 30 mA. EQE curves were characterized with a Newport QE measurement kit by

focusing a monochromatic beam of light onto the devices. The SEM images were taken from a Quanta 200 FEG environmental scanning electron microscope. For the TPV measurements, the device was serially connected to a digital oscilloscope (DOS-X 3104A) and the input impedance of the oscilloscope set to 1 MΩ to form the open-circuit conditions, respectively, for monitoring the charge density decay. The TPV was measured under 1 sun illumination. An attenuated UV laser pulse (SRS NL 100 Nitrogen Laser) was used as a small perturbation to the background illumination on the device. The laser-pulse-induced photovoltage variation ($\Delta V$) and the $V_{OC}$ are produced by the background illumination. The wavelength of the N$_2$ laser was 337 nm, the repeating frequency was ≈10 Hz, and the pulse width was less than 3.5 ns. For the TPC measurement, the device was serially connected to a digital oscilloscope (DOS-X 3104A) and the input impedance of the oscilloscope set to 50 Ω to form the short-circuit conditions, respectively. The TPC was measured under dark condition. The laser-pulse-induced photocurrent variation ($\Delta I$) is produced by the same pulse used in TPV test.

*TRPL Measurement*: A 404 nm pulsed diode laser with a pulse width of 45 ps was used to trigger the PL of perovskite film under ambient condition at room temperature. The excited PL was then collected by the TRPL spectroscopy from Horiba (DeltaPro). Based on the decay curve, a single exponential decay function was used to fit the decay to get the PL lifetime.

*DFT Calculation*: First-principles calculation was carried out in the framework of density functional theory as implemented in the VASP program. The generalized gradient approximation in the form of Perdew–Burke–Ernzerhof was used for the exchange–correlation function. The ion–electron interaction is treated with the projector-augmented wave method. Grimme's DFT-D3 correction is adopted to describe the long-range van der Waals interactions. Surface slab was modeled MAI-terminated symmetric (001) slabs of the tetragonal structure, which has a super cell of 2 × 2 and 9 layers of MAI and PbI$_2$ in total. About 30 Å vacuum was added on top of the slab surface to minimize the interaction between the adjacent slabs. Pb clusters are added to the top of the surfaces, which introduce defect states into the systems. An extra MAI layer was added in the cases of excess-MAI models. A 5 × 5 Monkhorst–Pack grid is used for all density of states calculations.

*t-DOS Measurement*: TAS is used to extract the energetic profile of trap density by the equation

$$N_T(E_\omega) = -\frac{V_{bi}}{qW}\frac{dC}{d\omega}\frac{\omega}{k_B T} \tag{1}$$

where $V_{bi}$ and $W$ are the build-in potential and depletion width, respectively, which were derived from Mott–Schottky analysis. $C$ is the capacitance, and $\omega$ is the angular frequency. And $q$ is the elementary charge. $k_B$ and $T$ are the Boltzmann's constant and temperature, respectively. The applied angular frequency $\omega$ defines an energetic demarcation

$$E_\omega = k_B T \ln\left(\frac{\omega_0}{\omega}\right) \tag{2}$$

where $\omega_0$ is the attempt-to-escape frequency. The trap states below the energy demarcation can capture or emit charges with the given $\omega$ and contribute to the capacitance.

## Supporting Information

Supporting Information is available from the Wiley Online Library or from the author.

## Acknowledgements

## Conflict of Interest

The authors declare no conflict of interest.

## Keywords

[1] S. D. Stranks, G. E. Eperon, G. Grancini, C. Menelaou, M. J. Alcocer, T. Leijtens, L. M. Herz, A. Petrozza, H. J. Snaith, *Science* **2013**, *342*, 341.

[2] C. Wehrenfennig, G. E. Eperon, M. B. Johnston, H. J. Snaith, L. M. Herz, *Adv. Mater.* **2014**, *26*, 1584.

[3] Z. Xiao, Y. Yuan, Q. Wang, Y. Shao, Y. Bai, Y. Deng, Q. Dong, M. Hu, C. Bi, J. Huang, *Mater. Sci. Eng. R* **2016**, *101*, 1.

[4] A. Kojima, K. Teshima, Y. Shirai, T. Miyasaka, *J. Am. Chem. Soc.* **2009**, *131*, 6050.

[5] W. S. Yang, J. H. Noh, N. J. Jeon, Y. C. Kim, S. Ryu, J. Seo, S. I. Seok, *Science* **2015**, *348*, 1234.

[6] M. A. Green, A. Ho-Baillie, H. J. Snaith, *Nat. Photonics* **2014**, *8*, 506.

[7] X. Zheng, B. Chen, J. Dai, Y. Fang, Y. Bai, Y. Lin, H. Wei, X. C. Zeng, J. Huang, *Nat. Energy* **2017**, *2*, 17102.

[8] M. Ahmadi, T. Wu, B. Hu, *Adv. Mater.* **2017**, *29*, 1605242.

[9] J. Huang, Y. Shao, Q. Dong, *J. Phys. Chem. Lett.* **2015**, *6*, 3218.

[10] H. Wei, Y. Fang, P. Mulligan, W. Chuirazzi, H.-H. Fang, C. Wang, B. R. Ecker, Y. Gao, M. A. Loi, L. Cao, *Nat. Photonics* **2016**, *10*, 333.

[11] Y. Fang, Q. Dong, Y. Shao, Y. Yuan, J. Huang, *Nat. Photonics* **2015**, *9*, 679.

[12] Y. Bai, Q. Dong, Y. Shao, Y. Deng, Q. Wang, L. Shen, D. Wang, W. Wei, J. Huang, *Nat. Commun.* **2016**, *7*, 12806.

[13] K. Chen, Q. Hu, T. Liu, L. Zhao, D. Luo, J. Wu, Y. Zhang, W. Zhang, F. Liu, T. P. Russell, R. Zhu, Q. Gong, *Adv. Mater.* **2016**, *28*, 10718.

[14] W. Chen, L. Xu, X. Feng, J. Jie, Z. He, *Adv. Mater.* **2017**, *29*, 1603923.

[15] C. Bi, Q. Wang, Y. Shao, Y. Yuan, Z. Xiao, J. Huang, *Nat. Commun.* **2015**, *6*, 7747.

[16] Z. Xiao, Q. Dong, C. Bi, Y. Shao, Y. Yuan, J. Huang, *Adv. Mater.* **2014**, *26*, 6503.

[17] H. Zhou, Q. Chen, G. Li, S. Luo, T.-b. Song, H.-S. Duan, Z. Hong, J. You, Y. Liu, Y. Yang, *Science* **2014**, *345*, 542.

[18] D. Luo, L. Zhao, J. Wu, Q. Hu, Y. Zhang, Z. Xu, Y. Liu, T. Liu, K. Chen, W. Yang, *Adv. Mater.* **2017**, *29*, 1604758.

[19] B. Wu, H. T. Nguyen, Z. Ku, G. Han, D. Giovanni, N. Mathews, H. J. Fan, T. C. Sum, *Adv. Energy Mater.* **2016**, *6*, 1600551.

[20] C. Bi, Y. Shao, Y. Yuan, Z. Xiao, C. Wang, Y. Gao, J. Huang, *J. Mater. Chem. A* **2014**, *2*, 18508.

[21] N. Ahn, D.-Y. Son, I.-H. Jang, S. M. Kang, M. Choi, N.-G. Park, *J. Am. Chem. Soc.* **2015**, *137*, 8696.

[22] Q. Wang, Q. Dong, T. Li, A. Gruverman, J. Huang, *Adv. Mater.* **2016**, *28*, 6734.

[23] A. G. Aberle, *Prog. Photovoltaics* **2000**, *8*, 473.

[24] B. Yan, G. Yue, L. Sivec, J. Yang, S. Guha, C.-S. Jiang, *Appl. Phys. Lett.* **2011**, *99*, 113512.

[25] Y. Liu, T. Lai, H. Li, Y. Wang, Z. Mei, H. Liang, Z. Li, F. Zhang, W. Wang, A. Y. Kuznetsov, *Small* **2012**, *8*, 1392.

[26] Y. Shao, Z. Xiao, C. Bi, Y. Yuan, J. Huang, *Nat. Commun.* **2014**, *5*, 5784.

[27] J. Xu, A. Buin, A. H. Ip, W. Li, O. Voznyy, R. Comin, M. Yuan, S. Jeon, Z. Ning, J. J. McDowell, *Nat. Commun.* **2015**, *6*, 7081.

[28] N. K. Noel, A. Abate, S. D. Stranks, E. S. Parrott, V. M. Burlakov, A. Goriely, H. J. Snaith, *ACS Nano* **2014**, *8*, 9815.

[29] J.-W. Lee, H.-S. Kim, N.-G. Park, *Acc. Chem. Res.* **2016**, *49*, 311.

[30] Y. Lin, L. Shen, J. Dai, Y. Deng, Y. Wu, Y. Bai, X. Zheng, J. Wang, Y. Fang, H. Wei, W. Ma, X. C. Zeng, X. Zhan, J. Huang, *Adv. Mater.* **2016**, *29*, 1604545.

[31] R. G. Pearson, *Science* **1966**, *151*, 172.

[32] T. Shi, W.-J. Yin, F. Hong, K. Zhu, Y. Yan, *Appl. Phys. Lett.* **2015**, *106*, 103902.

[33] Q. Wang, Y. Shao, H. Xie, L. Lyu, X. Liu, Y. Gao, J. Huang, *Appl. Phys. Lett.* **2014**, *105*, 163508.

[34] A. Dualeh, N. Tétreault, T. Moehl, P. Gao, M. K. Nazeeruddin, M. Grätzel, *Adv. Funct. Mater.* **2014**, *24*, 3250.

[35] Q. Chen, H. Zhou, T.-B. Song, S. Luo, Z. Hong, H.-S. Duan, L. Dou, Y. Liu, Y. Yang, *Nano Lett.* **2014**, *14*, 4158.

[36] D. O'kane, K. Mittal, *J. Vac. Sci. Technol.* **1974**, *11*, 567.

[37] J. V. d. Weide, R. Nemanich, *Appl. Phys. Lett.* **1993**, *62*, 1878.

[38] S. L. Buckles, *Proc. of the 5th International Microelectronics Conf.* **1988**, 383.

[39] Y. Shao, Y. Yuan, J. Huang, *Nat. Energy* **2016**, *1*, 15001.

[40] Y. Fang, C. Bi, D. Wang, J. Huang, *ACS Energy Lett.* **2017**, *2*, 782.

[41] R. Dong, Y. Fang, J. Chae, J. Dai, Z. Xiao, Q. Dong, Y. Yuan, A. Centrone, X. C. Zeng, Huang, *Adv. Mater.* **2015**, *27*, 1912.

[42] L. Shen, Y. Fang, D. Wang, Y. Bai, Y. Deng, M. Wang, Y. Lu, J. Huang, *Adv. Mater.* **2016**, *28*, 10794.

[43] H. Wei, Y. Fang, P. Mulligan, W. Chuirazzi, H.-H. Fang, C. Wang, B. R. Ecker, Y. Gao, M. A. Loi, L. Cao, *Nat. Photonics* **2016**, *10*, 333.

[44] Y. Yang, Y. Yan, M. Yang, S. Choi, K. Zhu, J. M. Luther, M. C. Beard, *Nat. Commun.* **2015**, *6*, 7961.

[45] Z. Chen, Q. Dong, Y. Liu, C. Bao, Y. Fang, Y. Lin, S. Tang, Q. Wang, X. Xiao, Y. Bai, Y. Deng, J. Huang, *Nat. Commun.* **2017**, *8*, 1890.

[46] C. Bao, Z. Chen, Y. Fang, H. Wei, Y. Deng, X. Xiao, L. Li, J. Huang, *Adv. Mater.* **2017**, *29*, 1703209.

[47] T. Walter, R. Herberholz, C. Müller, H. Schock, *J. Appl. Phys.* **1996**, *80*, 4411.

[48] C. Melzer, E. J. Koop, V. D. Mihailetchi, P. W. Blom, *Adv. Funct. Mater.* **2004**, *14*, 865.

[49] J. A. Carr, S. Chaudhary, *Energy Environ. Sci.* **2013**, *6*, 3414.

[50] Z. Xiao, C. Bi, Y. Shao, Q. Dong, Q. Wang, Y. Yuan, C. Wang, Y. Gao, J. Huang, *Energy Environ. Sci.* **2014**, *7*, 2619.

[51] Q. Wang, Y. Shao, Q. Dong, Z. Xiao, Y. Yuan, J. Huang, *Energy Environ. Sci.* **2014**, *7*, 2359.